

# A full vectorial contrast source inversion scheme for three-dimensional acoustic imaging of both compressibility and density profiles

Koen W. A. van Dongen<sup>a)</sup> and William M. D. Wright<sup>b)</sup>

Ultrasonics Research Group, Department of Electrical and Electronic Engineering, University College Cork, College Road, Cork, Ireland

(Received 3 August 2006; revised 6 December 2006; accepted 6 December 2006)

Imaging the two acoustic medium parameters density and compressibility requires the use of both the acoustic pressure and velocity wave fields, described via integral equations. Imaging is based on solving for the unknown medium parameters using known measured scattered wave fields, and it is difficult to solve this ill-posed inverse problem directly using a conjugate gradient inversion scheme. Here, a contrast source inversion method is used in which the contrast sources, defined via the product of changes in compressibility and density with the pressure and velocity wave fields, respectively, are computed iteratively. After each update of the contrast sources, an update of the medium parameters is obtained. Total variation as multiplicative regularization is used to minimize blurring in the reconstructed contrasts. The method successfully reconstructed three-dimensional contrast profiles based on changes in both density and compressibility, using synthetic data both with and without 50% white noise. The results were compared with imaging based only on the pressure wave field, where speed of sound profiles were solely based on changes in compressibility. It was found that the results improved significantly by using the full vectorial method when changes in speed of sound depended on changes in both compressibility and density. © 2007 Acoustical Society of America. [DOI: 10.1121/1.2431333]

PACS number(s): 43.60.Pt, 43.20.El, 43.20.Fn, 43.60.Uv, 43.80.Qf [TDM] Pages: 1538–1549

## I. INTRODUCTION

Ultrasonic tomographic imaging<sup>1–4</sup> is a well-established technique for medical diagnosis and other applications. One of the medical applications is to use ultrasound for imaging temperature distributions in the human body (e.g., Johnson *et al.*<sup>5</sup>) and in particular during high-temperature hyperthermia cancer treatments with high-intensity focused ultrasound (HIFU).<sup>6,7</sup> During this treatment, the tumor temperature is increased up to 50–55 °C for a duration of 1 or 2 min or for a shorter period of time at temperatures over 60 °C.<sup>8,9</sup> For efficient treatment, it is important to monitor the process by verifying (i) that the tumor temperature has become sufficiently high to induce cell necrosis, and (ii) that the healthy tissue surrounding the tumor remains at or near normal body temperature to prevent it from being damaged. The advantages of using ultrasound as a guidance method are that it is noninvasive, relatively cheap, and compatible with the HIFU apparatus.

Several techniques exist to estimate the tissue temperature from ultrasound. Some are based on thermally induced strain<sup>10–12</sup> while others are based on the observation that biological tissues can be described by semiregular lattices of which the scattering properties change as a function of temperature.<sup>13–17</sup>

Using acoustics for monitoring the process is a difficult task due to the fact that the changes in acoustic medium parameters between various soft tissues or between regions of the same tissue at different temperatures are relatively small. In liver tissue for example, a change in temperature from 37 °C to 50 °C typically produces a contrast in sound speed of only 6 m/s.<sup>10,11,18</sup> Consequently, a more sensitive imaging method utilizing through-transmission may be more appropriate,<sup>19</sup> which has also been used for temperature estimation.<sup>20,21</sup> These techniques typically operate with transient signals of which the frequency range is a compromise between using high enough frequencies to obtain adequate spatial resolution, and a low enough frequency content for adequate tissue penetration. The drawback of using low frequencies is that the corresponding wavelengths of the probing wave field are of the same order of magnitude as the spatial dimensions of the contrasts of interest, and effects like diffraction and multiple scattering between various regions with different medium parameters will occur. These effects are well described by utilizing the acoustic wave equations and using these wave equations for imaging is therefore an appropriate approach.<sup>22</sup> So far, the above methods do not employ the knowledge that these changes in speed of sound are not caused solely by changes in compressibility but by changes in both compressibility and volume density of mass. Hence, by doing so it is expected that the imaging results will improve, and this will be demonstrated in the work described here. While the motivation was to develop an imaging method for HIFU temperature moni-

<sup>a)</sup>Current address: Laboratory of Acoustical Imaging and Sound Control, Faculty of Applied Sciences, Delft University of Technology, The Netherlands. Electronic mail: k.w.a.vandongen@tudelft.nl

<sup>b)</sup>Electronic mail: bill.wright@ucc.ie

toring, the techniques described could easily be applied to any acoustic imaging problem containing small, weakly scattering contrasts.

The propagation and scattering of acoustic wave fields in the presence of acoustic contrasts is described via integral equations. These are obtained by combining the acoustic wave equations with reciprocity.<sup>23</sup> We refer to the forward problem where we solve the integral equation for the unknown total wave field in the case where we know the incident wave field and the contrast function. The inverse problem refers to the situation where the integral equation is solved for an unknown contrast function and known incident and scattered wave fields. Inspired by the success of conjugate gradient iterative solution methods for the forward problem,<sup>24,25</sup> a modified gradient inversion method has already been developed. With this method, the unknown contrast function was reconstructed from measured scattered wave fields with a conjugate gradient inversion scheme.<sup>26</sup> In order to tackle the blurring caused by noise in the data, the technique was extended by taking the total variation (TV) of the reconstructed contrast function into account.<sup>27–30</sup> The method was further improved by combining the contrast function with the total wave field leading to the introduction of source type integral equations (STIE),<sup>31</sup> and later on in combination with the modified gradient approach<sup>26,32,33</sup> to the contrast source (CS) method.<sup>34,35</sup> This has proven to be very successful, especially in combination with TV as a multiplicative regularizer for the electromagnetic,<sup>36</sup> elastodynamic,<sup>37</sup> and finally the acoustic scalar cases<sup>38</sup> where changes in density were neglected. Problems arise in situations where changes in speed of sound are not only due to changes in compressibility but also due to changes in density. In these situations, the acoustic scalar method is not sufficient and must be extended to a full vectorial method, which takes both the velocity and pressure wave fields into account. A full vectorial solution was presented in Refs. 39 and 40 for electromagnetics; here, we have developed a full vectorial scheme for the acoustic counterpart which meets the demands of reconstructing both density and compressibility profiles<sup>41</sup> and included an additional multiplicative regularization method based on minimization of the TV in the reconstructed contrast profiles. Contrary to the electromagnetic counterpart,<sup>39,40</sup> we normalize the error functionals using (i) a norm based on a combination of the pressure and velocity wave fields, and (ii) a norm which combines the presence of contrasts in both compressibility and density. Finally, we investigate the effect of the standard scalar approach on the reconstructed speed of sound profiles where changes in density are neglected.

## II. FORWARD PROBLEM

The forward and inverse problems are formulated in the temporal Laplace domain with Laplace parameter  $\hat{s}$ . Frequency domain results are obtained by taking the limit  $\hat{s} \rightarrow -i\omega$ , with  $i^2 = -1$  and where  $\omega \in \Omega$ , with  $\Omega$  the temporal angular frequency domain. The symbol “ $\wedge$ ” on top of a pa-

rameter is used to show its frequency dependency, whereas the vectors  $\mathbf{r}$  and  $\mathbf{r}'$  are used to notate a position in the three-dimensional spatial domain  $\mathbb{D}$ .

The propagation of acoustic wave fields is described via integral equations of the second type.<sup>23</sup> In the presence of acoustic contrasts, the total pressure and velocity wave fields  $\hat{p}^{\text{tot}}(\mathbf{r})$  and  $\hat{v}_i^{\text{tot}}(\mathbf{r})$  for  $\{i, j\} = 1, 2, \text{ or } 3$  equals

$$\hat{p}^{\text{tot}}(\mathbf{r}) = \hat{p}^{\text{inc}}(\mathbf{r}) + \hat{p}^{\text{sct}}(\mathbf{r}), \quad (1)$$

$$\hat{v}_i^{\text{tot}}(\mathbf{r}) = \hat{v}_i^{\text{inc}}(\mathbf{r}) + \hat{v}_i^{\text{sct}}(\mathbf{r}), \quad (2)$$

where  $\hat{p}^{\text{inc}}(\mathbf{r})$  and  $\hat{v}_i^{\text{inc}}(\mathbf{r})$  are the incident pressure and velocity wave fields and where  $\hat{p}^{\text{sct}}(\mathbf{r})$  and  $\hat{v}_i^{\text{sct}}(\mathbf{r})$  refer to the scattered pressure and velocity fields, respectively.

The scattered wave fields occur due to the presence of acoustic contrasts defined via the contrast functions  $\chi^{\kappa}(\mathbf{r}')$  and  $\chi^{\rho}(\mathbf{r}')$ , which read

$$\chi^{\kappa}(\mathbf{r}') = \kappa^{\text{bg}} - \kappa^{\text{obj}}(\mathbf{r}'), \quad (3)$$

$$\chi^{\rho}(\mathbf{r}') = \rho^{\text{bg}} - \rho^{\text{obj}}(\mathbf{r}'). \quad (4)$$

The superscripts “bg” and “obj” are used to refer to the background and object medium parameters, respectively, which we assume to be nondispersive. In addition, we define the following Green’s functions  $\hat{G}$  applied on a volume density of injection rate source  $\hat{q}(\mathbf{r}')$  or a volume density of force  $\hat{f}_j(\mathbf{r}')$  as follows:

$$\{\hat{G}^{pq}\hat{q}\}(\mathbf{r}) = \hat{s}\rho^{\text{bg}} \int_{\mathbf{r}' \in \mathbb{D}} \hat{G}(\mathbf{r}-\mathbf{r}') \hat{q}(\mathbf{r}') dV(\mathbf{r}'), \quad (5)$$

$$\{\hat{G}^{pf}\hat{f}_j\}(\mathbf{r}) = - \sum_j \partial_j \int_{\mathbf{r}' \in \mathbb{D}} \hat{G}(\mathbf{r}-\mathbf{r}') \hat{f}_j(\mathbf{r}') dV(\mathbf{r}'), \quad (6)$$

$$\{\hat{G}^{vq}\hat{q}\}_i(\mathbf{r}) = - \partial_i \int_{\mathbf{r}' \in \mathbb{D}} \hat{G}(\mathbf{r}-\mathbf{r}') \hat{q}(\mathbf{r}') dV(\mathbf{r}'), \quad (7)$$

$$\{\hat{G}^{vf}\hat{f}_j\}_i(\mathbf{r}) = \frac{1}{\hat{s}\rho^{\text{bg}}} \left[ \partial_i \sum_j \partial_j \int_{\mathbf{r}' \in \mathbb{D}} \hat{G}(\mathbf{r}-\mathbf{r}') \hat{f}_j(\mathbf{r}') dV(\mathbf{r}') + \sum_j \int_{\mathbf{r}' \in \mathbb{D}} \delta(\mathbf{r}-\mathbf{r}') \delta_{i,j} \hat{f}_j(\mathbf{r}') dV(\mathbf{r}') \right], \quad (8)$$

with  $\partial_i$  the spatial derivative in the  $x_i$  direction,  $\delta_{i,j}$  Kronecker’s delta function,  $\delta(\mathbf{r}-\mathbf{r}')$  the impulse response function,  $\hat{G}(\mathbf{r}-\mathbf{r}')$  the scalar form of Green’s function.<sup>23</sup>

It is well known that the scattered wave fields  $\hat{p}^{\text{sct}}(\mathbf{r})$  and  $\hat{v}_i^{\text{sct}}(\mathbf{r})$  read

$$\hat{p}^{\text{sct}}(\mathbf{r}) = \{\hat{G}^{pq}\hat{s}\chi^{\kappa}\hat{p}^{\text{tot}}\}(\mathbf{r}) + \{\hat{G}^{pf}\hat{s}\chi^{\rho}\hat{v}_j^{\text{tot}}\}(\mathbf{r}), \quad (9)$$

$$\hat{v}_i^{\text{sct}}(\mathbf{r}) = \{\hat{G}^{vq}\hat{s}\chi^{\kappa}\hat{p}^{\text{tot}}\}_i(\mathbf{r}) + \{\hat{G}^{vf}\hat{s}\chi^{\rho}\hat{v}_j^{\text{tot}}\}_i(\mathbf{r}), \quad (10)$$

which can be proved by using reciprocity.<sup>23</sup> Equations (9) and (10) form an integral equation which can be solved numerically for known contrast functions and unknown total wave fields.<sup>22</sup>

The above vectorial formulation can be reduced to a scalar formulation by assuming that there is only a contrast in compressibility. This leads to the following expression for the total pressure wave field:

$$\hat{p}^{\text{tot}}(\mathbf{r}) = \hat{p}^{\text{inc}}(\mathbf{r}) + \hat{s}^2 \int_{\mathbf{r}' \in \mathcal{D}} \hat{G}(\mathbf{r} - \mathbf{r}') \times \left( \frac{1}{[c^{\text{bg}}]^2} - \frac{1}{[c^{\text{obj}}(\mathbf{r}')]^2} \right) \hat{p}^{\text{tot}}(\mathbf{r}') dV(\mathbf{r}'), \quad (11)$$

with  $[c^{\text{bg}}]^2 = 1/[\kappa^{\text{bg}}\rho^{\text{bg}}]$  and  $[c^{\text{obj}}(\mathbf{r}')]^2 = 1/[\kappa^{\text{obj}}(\mathbf{r}')\rho^{\text{bg}}]$ . This very same result is obtained if we use the scalar wave equation as the starting point. Note that the situation where there is only a contrast in density will lead to a scattered velocity wave field only, which is independent of the pressure wave field.

### III. INVERSE PROBLEM AND CONTRAST SOURCE FORMULATION

The inverse problem refers to the situation where the unknown contrast function is computed. Here, we make use of the knowledge we have about the incident wave field everywhere in the region of interest and the measured scattered wave field at a limited number of receiver positions. For the acoustic case this results in the reconstruction of the acoustic medium parameters compressibility  $\kappa$  and density  $\rho$  by solving the set of integral equations stated in Eqs. (1)–(8).

Various methods exist to solve this problem within the Born or Rytov approximation.<sup>42–45</sup> However, this approximation only works as long as multiple scattering can be neglected and the scatterers themselves are weak. Improvements can be expected by employing the distorted Born iteration method;<sup>46</sup> however, this still involves utilizing an approximation to the formal solution of the inverse problem. Hence, research has been conducted towards methods which go beyond the Born approximation and which do not require solution of the forward problem after each update of the contrast function.

Due to the ill-posed nature of the inverse problem, it cannot be solved with a standard conjugate gradient (CG) inversion scheme, and regularization is required. This regularization is obtained by using a contrast source (CS) formulation as applied to, amongst others, electromagnetic scattering problems.<sup>34,35</sup> This formulation leads to the introduction of two, instead of one, error functionals which are minimized iteratively with an adapted CG inversion scheme. Although the problem remains ill-posed,<sup>47</sup> the approach has proven to be very effective in many inversion procedures.<sup>31</sup> Additional regularization is obtained by minimizing the TV present in the reconstructed contrast functions.<sup>36–39</sup> The full electromagnetic scattering problem, where contrasts in both complex permittivity and permeability are present, has been investigated previously;<sup>39</sup> here, we investigate the full vectorial acoustic counterpart. We first formulate the inverse problem based on the full vectorial acoustic problem. We then investigate the simplified scalar wave field problem by neglecting changes in mass density which are related to the velocity wave field.

Examining Eqs. (9) and (10) reveals that there are two source types that generate the scattered wave fields: sources defined via the product of changes in compressibility with the total pressure wave field, and sources defined via the product of changes in density with the velocity wave fields. This leads to the introduction of the contrast sources  $\hat{w}_k^p(\mathbf{r})$  and  $\hat{w}_{i,k}^v(\mathbf{r})$ , which are defined as

$$\hat{w}_k^p(\mathbf{r}) = \hat{s}\chi^\kappa(\mathbf{r})\hat{p}_k^{\text{tot}}(\mathbf{r}), \quad (12)$$

$$\hat{w}_{i,k}^v(\mathbf{r}) = \hat{s}\chi^\rho(\mathbf{r})\hat{v}_{i,k}^{\text{tot}}(\mathbf{r}), \quad (13)$$

where the subscript  $k=1, \dots, K$  refers to the discrete spatial positions of the transmitter which generates the incident wave fields. Consequently, the scattered wave fields formulated in Eqs. (9) and (10) are a function of the contrast sources  $\hat{w}_k^p(\mathbf{r})$  and  $\hat{w}_{i,k}^v(\mathbf{r})$ , and equal

$$\hat{p}_k^{\text{sct}}(\mathbf{r}) = \{\hat{\mathcal{G}}^{pq}\hat{w}_k^p(\mathbf{r}) + \{\hat{\mathcal{G}}^{pf}\hat{w}_{j,k}^v(\mathbf{r})\}(\mathbf{r}), \quad (14)$$

$$\hat{v}_{i,k}^{\text{sct}}(\mathbf{r}) = \{\hat{\mathcal{G}}^{vq}\hat{w}_{ji}^p(\mathbf{r}) + \{\hat{\mathcal{G}}^{vf}\hat{w}_{j,k}^v(\mathbf{r})\}(\mathbf{r}). \quad (15)$$

Combining Eqs. (12)–(15) leads to an expression of the contrast sources which reads

$$\hat{w}_k^p(\mathbf{r}) = \hat{s}\chi^\kappa(\mathbf{r})\hat{p}_k^{\text{inc}}(\mathbf{r}) + \hat{s}\chi^\kappa(\mathbf{r})\{\hat{\mathcal{G}}^{pq}\hat{w}_k^p(\mathbf{r}) + \hat{s}\chi^\kappa(\mathbf{r}) \times \{\hat{\mathcal{G}}^{pf}\hat{w}_{j,k}^v(\mathbf{r})\}(\mathbf{r}), \quad (16)$$

$$\hat{w}_{i,k}^v(\mathbf{r}) = \hat{s}\chi^\rho(\mathbf{r})\hat{v}_{i,k}^{\text{inc}}(\mathbf{r}) + \hat{s}\chi^\rho(\mathbf{r})\{\hat{\mathcal{G}}^{vq}\hat{w}_{ji}^p(\mathbf{r}) + \hat{s}\chi^\rho(\mathbf{r}) \times \{\hat{\mathcal{G}}^{vf}\hat{w}_{j,k}^v(\mathbf{r})\}(\mathbf{r}). \quad (17)$$

Next, Eqs. (12)–(17) are used to formulate two sets of error functionals. The first one is referred to as the error in the data equation and is based on the residual of the measured scattered wave fields minus the computed scattered wave fields based on the approximated contrast sources. Hence, at the  $N$ th iteration step these error functionals read

$$\hat{r}_{S;N;k}^p(\mathbf{r}) = \hat{p}_k^{\text{sct}}(\mathbf{r}) - \{\hat{\mathcal{G}}_S^{pq}\hat{w}_{N;k}^p(\mathbf{r}) - \{\hat{\mathcal{G}}_S^{pf}\hat{w}_{N;j;k}^v(\mathbf{r})\}(\mathbf{r}) \quad \forall \mathbf{r} \in S, \quad (18)$$

$$\hat{r}_{S;N;i,k}^v(\mathbf{r}) = \hat{v}_{i,k}^{\text{sct}}(\mathbf{r}) - \{\hat{\mathcal{G}}_S^{vq}\hat{w}_{N;j;k}^p(\mathbf{r}) - \{\hat{\mathcal{G}}_S^{vf}\hat{w}_{N;j;k}^v(\mathbf{r})\}(\mathbf{r}) \quad \forall \mathbf{r} \in S, \quad (19)$$

with  $S$  the spatial domain containing the transducers. The second one is referred to as the error in the object equation and is based on the error in the computed contrast sources. Consequently, these error functionals equal

$$\begin{aligned} \hat{r}_{D;N;k}^p(\mathbf{r}) &= \hat{s}\chi_N^k(\mathbf{r})\hat{p}_k^{\text{inc}}(\mathbf{r}) + \hat{s}\chi_N^k(\mathbf{r})\{\hat{G}^{pq}w_k^p\}(\mathbf{r}) \\ &+ \hat{s}\chi_N^k(\mathbf{r})\{\hat{G}^{pf}\hat{w}_{N;j;k}^v\}(\mathbf{r}) - \hat{w}_{N;k}^p(\mathbf{r}) \quad \forall \mathbf{r} \in \mathbb{D}, \end{aligned} \quad (20)$$

$$\begin{aligned} \hat{r}_{D;N;i,k}^v(\mathbf{r}) &= \hat{s}\chi_N^p(\mathbf{r})\hat{v}_{i,k}^{\text{inc}}(\mathbf{r}) + \hat{s}\chi_N^p(\mathbf{r})\{\hat{G}^{vq}w_k^p\}(\mathbf{r}) \\ &+ \hat{s}\chi_N^p(\mathbf{r})\{\hat{G}^{vf}\hat{w}_{N;j,k}^v\}(\mathbf{r}) - \hat{w}_{N;i,k}^v(\mathbf{r}) \quad \forall \mathbf{r} \in \mathbb{D}, \end{aligned} \quad (21)$$

with  $\mathbb{D}$  the spatial domain containing the contrasts and contrast sources.

## A. UPDATE OF THE CONTRAST SOURCES

For given contrast sources  $w_{N;k}^p(\mathbf{r})$  and  $w_{N;j,k}^v(\mathbf{r})$  and contrasts  $\chi_N^p(\mathbf{r})$  and  $\chi_N^v(\mathbf{r})$ , in each iteration, a single step in a CG scheme with Polak-Ribière update directions is employed to update the contrast sources<sup>39,40</sup> where updating of the contrast sources and the contrasts occurs in an alternating fashion. The update direction for the contrast sources in the inversion scheme depends on the definition of the norm of a vector. Contrary to the method described in Refs. 39 and 40, which uses two separate norms for each wave field quantity based solely on each wave field quantity, we propose to use a combined  $L_2$  norm of the four-dimensional vector representing the acoustic wave fields in the spatial domain  $\mathbb{S}$ . This improves the weighting and normalizing of the field quantities and consequently our method will perform better, especially in situations where the contrast in density is considerably smaller (or larger) than the contrast in the compressibility. Hence, the  $L_2$  norm of the combined pressure and velocity wave fields equals

$$\left\| \begin{matrix} \hat{p}_k(\mathbf{r}) \\ \hat{v}_{i,k}(\mathbf{r}) \end{matrix} \right\|_{\mathbb{S}}^2 = \sum_{\mathbf{r} \in \mathbb{S},k,\Omega} \left[ Z\hat{p}_k(\mathbf{r})\overline{\hat{p}_k(\mathbf{r})} + \sum_i \hat{v}_{i,k}(\mathbf{r})\overline{\hat{v}_{i,k}(\mathbf{r})} \right], \quad (22)$$

where the lines over the quantities  $\hat{p}_k(\mathbf{r})$  and  $\hat{v}_{i,k}(\mathbf{r})$  are used to denote that the complex conjugate is taken, whereas the  $L_2$  norm of a four-dimensional vector representing the contrast sources in the spatial domain  $\mathbb{D}$  reads

$$\left\| \begin{matrix} \hat{w}_k^p(\mathbf{r}) \\ \hat{w}_{i,k}^v(\mathbf{r}) \end{matrix} \right\|_{\mathbb{D}}^2 = \sum_{\mathbf{r} \in \mathbb{D},k,\Omega} \left[ Z\hat{w}_k^p(\mathbf{r})\overline{\hat{w}_k^p(\mathbf{r})} + \sum_i Z\hat{w}_{i,k}^v(\mathbf{r})\overline{\hat{w}_{i,k}^v(\mathbf{r})} \right]. \quad (23)$$

Note that we use the constant  $Z$  to correct for differences in the dimensions between the pressure and velocity wave field; consequently,  $Z$  is defined as

$$Z = \frac{\kappa^{\text{bg}}}{\rho^{\text{bg}}}. \quad (24)$$

Finally, we define the normalized error functional  $\text{Err}_N^{\text{SD}}$  at the  $N$ th iteration step as

$$\text{Err}_N^{\text{SD}} = \frac{\left\| \hat{r}_{S;N;k}^p(\mathbf{r}) \right\|_{\mathbb{S}}^2 + \left\| \hat{r}_{D;N;k}^p(\mathbf{r}) \right\|_{\mathbb{D}}^2}{\left\| \hat{p}_k^{\text{sct}}(\mathbf{r}) \right\|_{\mathbb{S}}^2 + \left\| \hat{s}\chi_{N-1}^k(\mathbf{r})\hat{p}_k^{\text{inc}}(\mathbf{r}) \right\|_{\mathbb{S}}^2} + \frac{\left\| \hat{r}_{S;N;i,k}^v(\mathbf{r}) \right\|_{\mathbb{S}}^2 + \left\| \hat{r}_{D;N;i,k}^v(\mathbf{r}) \right\|_{\mathbb{D}}^2}{\left\| \hat{v}_{i,k}^{\text{sct}}(\mathbf{r}) \right\|_{\mathbb{S}}^2 + \left\| \hat{s}\chi_{N-1}^p(\mathbf{r})\hat{v}_{i,k}^{\text{inc}}(\mathbf{r}) \right\|_{\mathbb{S}}^2}, \quad (25)$$

with  $\chi_{N-1}^k(\mathbf{r})$  and  $\chi_{N-1}^p(\mathbf{r})$  based on the approximated medium parameters of the objects. These medium parameters are obtained from the contrast sources as discussed in the next section.

## B. UPDATE OF DENSITY AND COMPRESSIBILITY PROFILES FROM CONTRAST SOURCES

Profiles of the contrasts in compressibility and density are obtained from the contrast sources in an alternating fashion; after each update of the contrast sources, the contrasts  $\chi_N^k(\mathbf{r})$  and  $\chi_N^p(\mathbf{r})$  are computed by minimizing the error in the contrast sources defined in Eqs. (12) and (13). Direct minimization<sup>48</sup> of the  $L_2$  norm of the error functionals based on these definitions leads to the following expressions for the medium parameters of the objects which read

$$\kappa_N^{\text{obj}}(\mathbf{r}) = \kappa^{\text{bg}} - \frac{\sum_{k,\Omega} \Re[\hat{s}\hat{p}_{N;k}^{\text{tot}}(\mathbf{r})\overline{\hat{w}_{N;k}^p(\mathbf{r})}]}{\sum_{k,\Omega} |\hat{s}\hat{p}_{N;k}^{\text{tot}}(\mathbf{r})|^2}, \quad (26)$$

$$\rho_N^{\text{obj}}(\mathbf{r}) = \rho^{\text{bg}} - \frac{\sum_{i,k,\Omega} \Re[\hat{s}\hat{v}_{N;i,k}^{\text{tot}}(\mathbf{r})\overline{\hat{w}_{N;i,k}^v(\mathbf{r})}]}{\sum_{i,k,\Omega} |\hat{s}\hat{v}_{N;i,k}^{\text{tot}}(\mathbf{r})|^2}. \quad (27)$$

However, if we explicitly assume the medium parameters to be real and non-negative, and multiply both sides of Eqs. (12) and (13) with  $[\hat{s}\hat{p}_{N;k}^{\text{tot}}(\mathbf{r})\hat{s}\hat{p}_{N;k}^{\text{tot}}(\mathbf{r})]/|\hat{s}\hat{p}_{N;k}^{\text{tot}}(\mathbf{r})|^M$  and  $[\hat{s}\hat{v}_{N;i,k}^{\text{tot}}(\mathbf{r})\hat{s}\hat{v}_{N;i,k}^{\text{tot}}(\mathbf{r})]/|\hat{s}\hat{v}_{N;i,k}^{\text{tot}}(\mathbf{r})|^M$ , respectively, the following expressions for  $\kappa_N^{\text{obj}}(\mathbf{r})$  and  $\rho_N^{\text{obj}}(\mathbf{r})$  are obtained:

$$\begin{aligned} \kappa_N^{\text{obj}}(\mathbf{r}) &= \left( \frac{\sum_{k,\omega} \left\{ \Re \left[ (\hat{w}_{N;k}^p(\mathbf{r}) - \hat{s}\kappa^{\text{bg}}\hat{p}_{N;k}^{\text{tot}}(\mathbf{r})) \frac{\overline{\hat{s}\hat{p}_{N;k}^{\text{tot}}(\mathbf{r})}}{|\hat{s}\hat{p}_{N;k}^{\text{tot}}(\mathbf{r})|^M} \right] \right\}^2 \right)^{1/2}}{\sum_{k,\omega} \left\{ \Re \left[ \frac{\hat{s}\hat{p}_{N;k}^{\text{tot}}(\mathbf{r})\overline{\hat{s}\hat{p}_{N;k}^{\text{tot}}(\mathbf{r})}}{|\hat{s}\hat{p}_{N;k}^{\text{tot}}(\mathbf{r})|^M} \right] \right\}^2} \right), \end{aligned} \quad (28)$$

$$\begin{aligned} \rho_N^{\text{obj}}(\mathbf{r}) &= \left( \frac{\sum_{i,k,\omega} \left\{ \Re \left[ (\hat{w}_{N;i,k}^v(\mathbf{r}) - \hat{s}\rho^{\text{bg}}\hat{v}_{N;i,k}^{\text{tot}}(\mathbf{r})) \frac{\overline{\hat{s}\hat{v}_{N;i,k}^{\text{tot}}(\mathbf{r})}}{|\hat{s}\hat{v}_{N;i,k}^{\text{tot}}(\mathbf{r})|^M} \right] \right\}^2 \right)^{1/2}}{\sum_{i,k,\omega} \left\{ \Re \left[ \frac{\hat{s}\hat{v}_{N;i,k}^{\text{tot}}(\mathbf{r})\overline{\hat{s}\hat{v}_{N;i,k}^{\text{tot}}(\mathbf{r})}}{|\hat{s}\hat{v}_{N;i,k}^{\text{tot}}(\mathbf{r})|^M} \right] \right\}^2} \right), \end{aligned} \quad (29)$$

where  $M$  can be chosen to be 1 or 2.



### C. REGULARIZATION WITH MULTIPLICATIVE TOTAL VARIATION

In situations where the data contain noise, additional regularization is preferable to stabilize the inversion process and to diminish the blurring in the reconstructed image. Results obtained with the CG-CS method are improved by applying regularization based on minimization of the TV in the reconstructed contrast profiles.<sup>36–39</sup> This is based on the knowledge that the objects under investigation are embedded in a homogeneous background medium, and that the amount of transient fluctuations is small. Implementation of this regularization is done by multiplying the error functional  $\text{Err}_N^{\text{SD}}$  as defined in Eq. (25) with an additional term that depends solely on the TV in the reconstructed contrasts. Consequently, we obtain a new error function  $\text{Err}_N$  which equals

$$\text{Err}_N = \text{Err}_N^{\text{SD}} \text{Err}_N^{\text{TV}}, \quad (30)$$

where  $\text{Err}_N^{\text{TV}}$  is a weighted  $L_2$  norm of the gradient of the contrast functions and equals

$$\text{Err}_N^{\text{TV}} = \int_{\mathbf{r} \in \mathbf{D}} \left[ \frac{|\nabla \chi_N^{\kappa}(\mathbf{r})|^2 + \delta_N^{\kappa}}{b_N^{\kappa}} + \frac{|\nabla \chi_N^{\rho}(\mathbf{r})|^2 + \delta_N^{\rho}}{b_N^{\rho}} \right] dV(\mathbf{r}), \quad (31)$$

with

$$b_N^{\kappa}(\mathbf{r}) = V(|\nabla \chi_{N-1}^{\kappa}(\mathbf{r})|^2 + \delta_N^{\kappa}), \quad (32)$$

$$b_N^{\rho}(\mathbf{r}) = V(|\nabla \chi_{N-1}^{\rho}(\mathbf{r})|^2 + \delta_N^{\rho}), \quad (33)$$

where  $V$  equals the volume of the spatial domain  $\mathbf{D}$ ,  $\nabla \chi_N^{\kappa}(\mathbf{r})$  and  $\nabla \chi_N^{\rho}(\mathbf{r})$  equal the gradients of the reconstructed compressibility and density, respectively, and where  $\delta_N^{\kappa}$  and  $\delta_N^{\rho}$  are used to restore the differentiability of the TV factor. Good results are obtained with the following choices for  $\delta_N^{\kappa}$  and  $\delta_N^{\rho}$ :

$$\delta_N^{\kappa} = \frac{\theta \text{Err}_N^{\text{SD}} (\kappa^{\text{bg}})^2}{(\Delta V)^{2/3}}, \quad (34)$$

$$\delta_N^{\rho} = \frac{\theta \text{Err}_N^{\text{SD}} (\rho^{\text{bg}})^2}{(\Delta V)^{2/3}}, \quad (35)$$

with steering parameter  $\theta$  controlling the reduction of the transient fluctuations in the reconstructed image; the lower the value, the larger the influence of the TV factor in the reconstruction process and the smoother the image becomes. This choice is based on the knowledge that  $|\nabla \chi_{N-1}^{\text{obj}}(\mathbf{r})|^2$  and  $|\nabla \rho_{N-1}^{\text{obj}}(\mathbf{r})|^2$  are of the order of  $(\kappa^{\text{bg}})^2 (\Delta V)^{-2/3}$  and  $(\rho^{\text{bg}})^2 (\Delta V)^{-2/3}$ . The influence of the TV factor should be increased during the inversion process when the system becomes increasingly sensitive to noise present in the data; hence, the factor  $\text{Err}_N^{\text{SD}}$  is added to obtain this effect; the overall desired effect with the TV factor depends on the amount of transient fluctuations permitted in the image, which is based for example on the noise present in the data. Consequently, a separate steering parameter  $\theta$  is needed which takes this into account. Typical values for  $\theta$  are in the range  $\theta = [10^{-3}, 10^0]$ . Note that the choice of our  $\delta_N^{\kappa}$  and  $\delta_N^{\rho}$  is

TABLE I. The medium parameters compressibility,  $\kappa$ , volume density of mass,  $\rho$ , and speed of sound,  $c$ , for human liver tissues at  $T=37, 45$ , and  $50$  °C.

	Compressibility $\kappa [10^{-9}(\text{Pa})^{-1}]$	Density $\rho [\text{kg/m}^3]$	Speed of sound $c [\text{m/s}]$
Liver at 37 °C	0.366 48	1056.6	1607
Liver at 45 °C	0.365 36	1053.3	1612
Liver at 50 °C	0.365 71	1051.0	1613

different from the one chosen in Refs. 39 and 49. Here, contrast source inversion is investigated for the electromagnetic case where changes in electric permittivity and conductivity, and magnetic permeability are present. Based on their formulations,  $\delta_N^{\kappa}$  and  $\delta_N^{\rho}$  would read

$$\delta_N^{\kappa} = \frac{\left( \frac{\|\hat{\rho}_{\mathbf{D};N;k}^{\rho}(\mathbf{r})\|_{\mathbf{D}}^2}{\|\hat{\chi}_{N-1}^{\kappa}(\mathbf{r}) \hat{p}_k^{\text{inc}}(\mathbf{r})\|_{\mathbf{D}}^2} \right)}{[\max(\Delta x_1, \Delta x_2, \Delta x_3)]^2}, \quad (36)$$

$$\delta_N^{\rho} = \frac{\left( \frac{\|\hat{\rho}_{\mathbf{D};N;i,k}^{\rho}(\mathbf{r})\|_{\mathbf{D}}^2}{\|\hat{\chi}_{N-1}^{\rho}(\mathbf{r}) \hat{v}_{i,k}^{\text{inc}}(\mathbf{r})\|_{\mathbf{D}}^2} \right)}{[\max(\Delta x_1, \Delta x_2, \Delta x_3)]^2}, \quad (37)$$

which is disadvantageous in the situations where the error and/or changes in density are considerably larger or smaller than the error and/or changes in compressibility. In addition, the parameters  $(\kappa^{\text{bg}})^2$  and  $(\rho^{\text{bg}})^2$  are omitted in their formulations since they work with normalized contrasts.

Minimization of the error functional  $\text{Err}_N^{\text{TV}}$  leads to the following updating scheme for the reconstructed acoustic medium parameters:

$$\chi_N^{\kappa, \text{TV}}(\mathbf{r}) = \chi_N^{\kappa}(\mathbf{r}) + \beta_N^{\kappa} g_N^{\kappa}(\mathbf{r}), \quad (38)$$

$$\chi_N^{\rho, \text{TV}}(\mathbf{r}) = \chi_N^{\rho}(\mathbf{r}) + \beta_N^{\rho} g_N^{\rho}(\mathbf{r}), \quad (39)$$

with update directions  $g_N^{\kappa}(\mathbf{r})$  and  $g_N^{\rho}(\mathbf{r})$  equal to

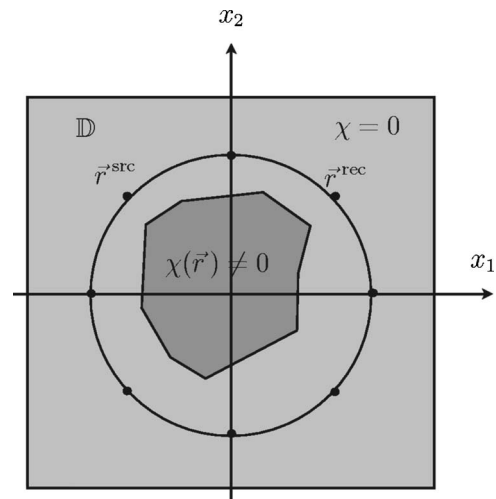


FIG. 1. The setup used for measurements. The transmitter and receiver positions are denoted by  $\mathbf{r}^{\text{src}}$  and  $\mathbf{r}^{\text{rec}}$ , whereas  $\chi(\mathbf{r})$  are the contrast functions.

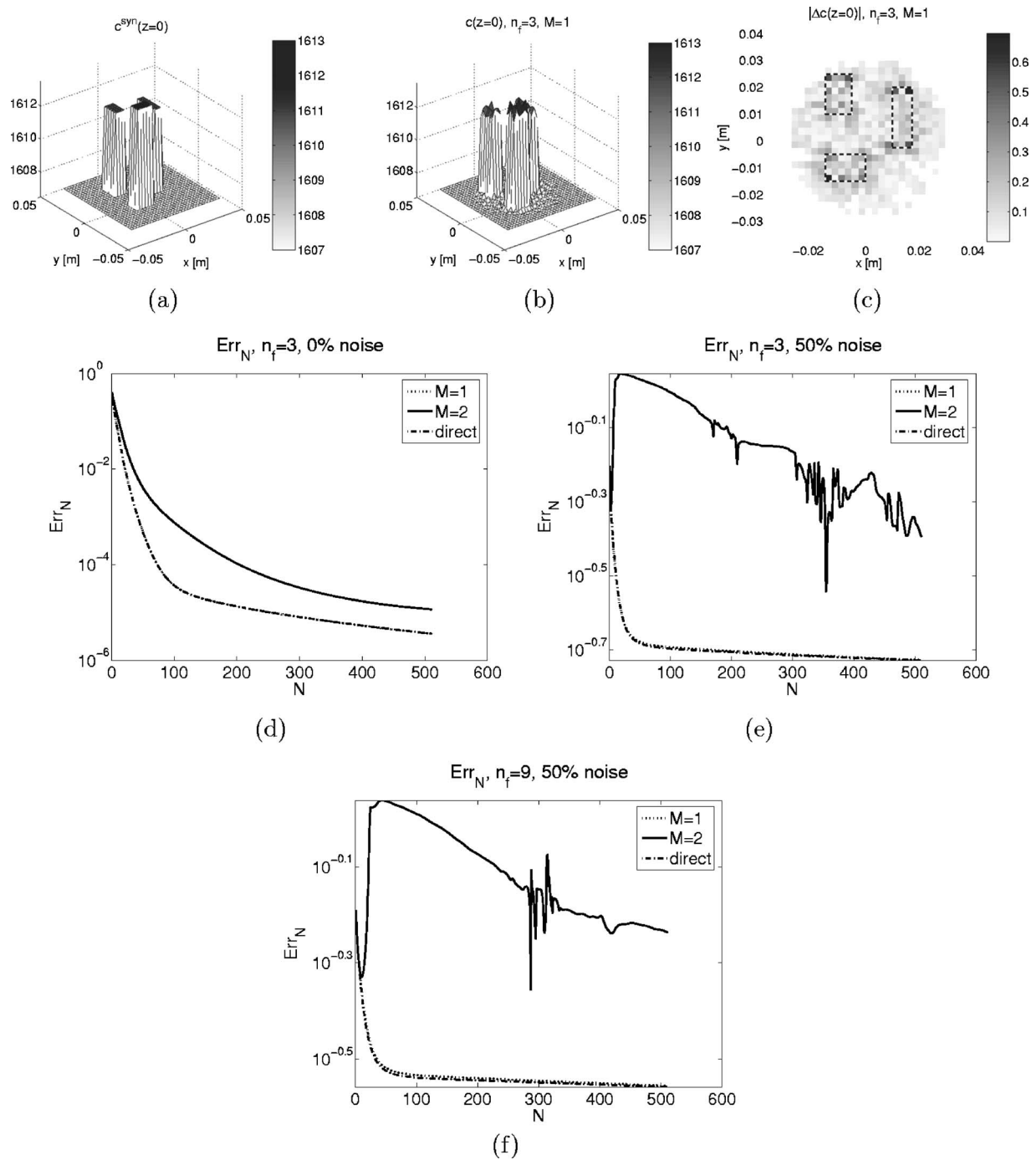


FIG. 2. Cross sections of the (a) synthetic and (b) reconstructed speed of sound profiles  $c(\mathbf{r})$  at  $z=0$  m and the absolute error  $|\Delta c(\mathbf{r})|$  in the computed speed of sound profile; (d)–(f) the error functionals  $\text{Err}_N$  for  $n_f=$  three and nine frequency components, without and with noise. The synthetic pressure wave field and the imaging are based on changes in the compressibility only.

$$g_N^\kappa(\mathbf{r}) = -2 \nabla \cdot \left[ \frac{\nabla \chi_{N-1}^\kappa(\mathbf{r})}{b_N^\kappa} \right], \quad (40)$$

$$g_N^\rho(\mathbf{r}) = -2 \nabla \cdot \left[ \frac{\nabla \chi_{N-1}^\rho(\mathbf{r})}{b_N^\rho} \right]. \quad (41)$$

The amplitudes of the update directions are chosen such that a maximum minimization of the error functional  $\text{Err}_N$  is obtained; hence,

$$\beta_N^\kappa = \arg \min_{\text{real } \beta^\kappa} \{ \text{Err}_N[\chi_N^\kappa(\mathbf{r}) + \beta_N^\kappa g_N^\kappa(\mathbf{r}), \chi_N^\rho(\mathbf{r})] \}, \quad (42)$$

$$\beta_N^\rho = \arg \min_{\text{real } \beta^\rho} \{ \text{Err}_N[\chi_N^\kappa(\mathbf{r}), \chi_N^\rho(\mathbf{r}) + \beta_N^\rho g_N^\rho(\mathbf{r})] \}. \quad (43)$$

This results in a fourth-degree polynomial in  $\beta_N^\kappa$  and a second one in  $\beta_N^\rho$  which can both be solved analytically.<sup>49</sup> Note that, after we have obtained the contrast functions  $\chi_N^{\kappa;\text{TV}}(\mathbf{r})$  and  $\chi_N^{\rho;\text{TV}}(\mathbf{r})$ , we update the contrasts sources with  $\chi_N^\kappa(\mathbf{r}) = \chi_N^{\kappa;\text{TV}}(\mathbf{r})$  and  $\chi_N^\rho(\mathbf{r}) = \chi_N^{\rho;\text{TV}}(\mathbf{r})$ . Note that the effect of multiplicative regularization on the inversion scheme was investigated earlier by Van den Berg *et al.*<sup>35</sup>

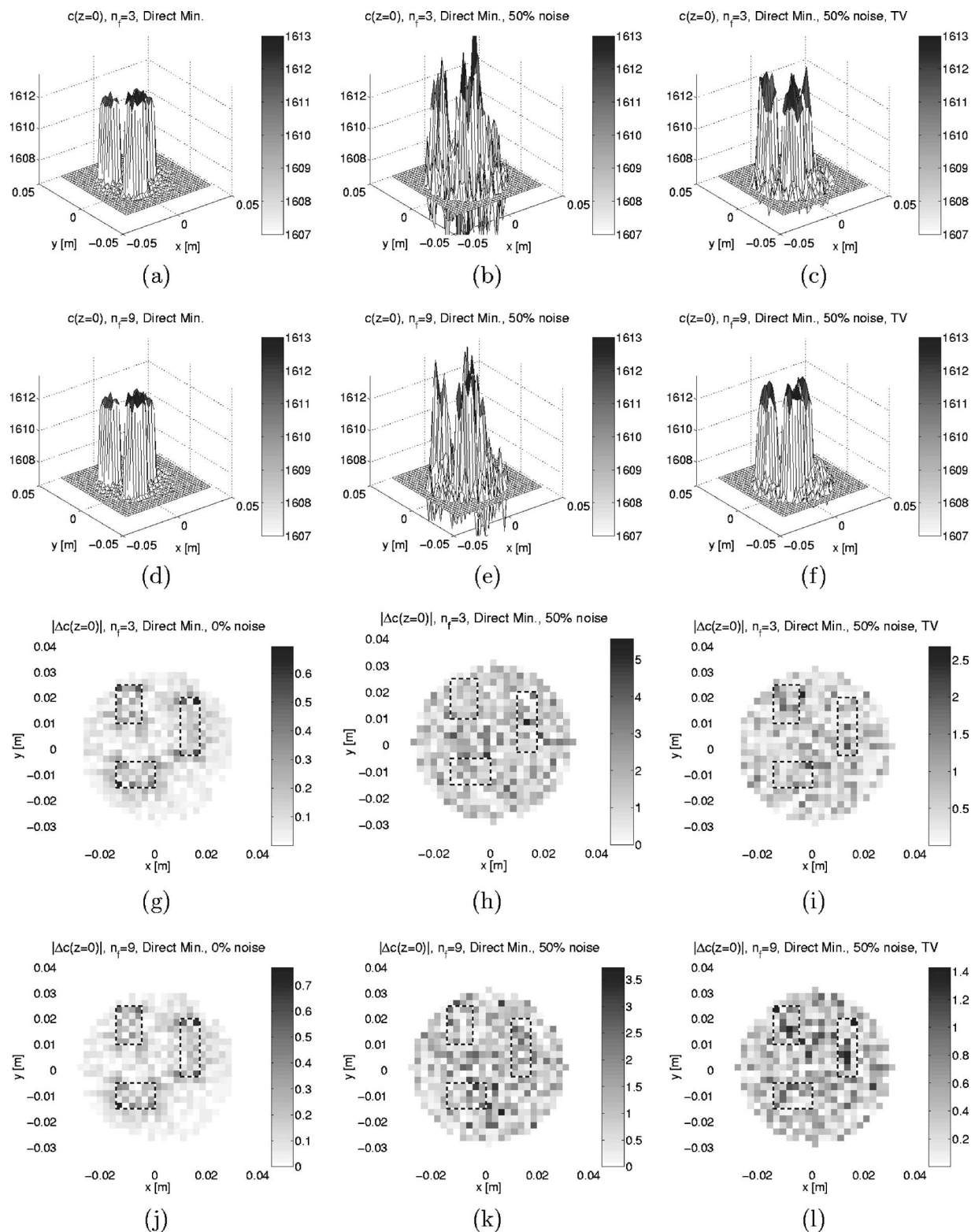


FIG. 3. Cross sections of the reconstructed speed of sound profiles  $c(\mathbf{r})$  at  $z=0$  m based on direct minimization and the absolute errors  $|\Delta c(\mathbf{r})|$ . The imaging is based on direct minimization (direct min.), direct minimization when noise is present, and direct minimization with total variation (TV) when noise is present. For all cases the situation is shown when either three or nine frequencies are used. The synthetic pressure wave field and the imaging are based on changes in the compressibility only.

#### IV. RESULTS AND DISCUSSION

Synthetic data were obtained by solving the forward problem<sup>22,50</sup> for medium parameters representing homogeneous human liver tissue at 37 °C containing three heated lesions, two at 45 °C and one at 50 °C. Note that the tech-

nique could be applied to any acoustical configuration in principle. The corresponding medium parameters are given in Table I and were obtained by combining results presented in the literature.<sup>18,10,11</sup> Note that the change in speed of sound due to heating is relatively small, *viz.*, 5 m/s between 37 °C

and 45 °C and 1 m/s between 45 °C and 50 °C. All media were assumed to be nondispersive and lossless. These losses could be included by taking complex instead of real values for the contrasts, such that the imaginary parts refer to the losses. The three-dimensional cylindrical volume contained  $32 \times 32 \times 4$  cubic elements of size  $2.5 \times 2.5 \times 2.5$  mm<sup>3</sup>. By choosing the number of elements to be a power of two in each direction, the usage of fast Fourier transform (FFTs) becomes feasible to compute the spatial convolutions efficiently. The frequency range of the transient signal was from 5 up to 156 kHz, which has corresponding wavelengths in the range of 10–320 mm. It will be shown that reliable imaging of small contrasts of approximately 2.5 mm in size is possible at these frequencies.

The synthetic data set is based on a tomographic setup as shown in Fig. 1, where 36 transducers are positioned circumferentially around the circular region of interest, in the plane  $z=0$  m. During the imaging, it was assumed that there was no contrast outside the circular cylindrical volume enclosed by the transducers. Increasing the number of transducers did little to improve the results, while it resulted in a large increase in the computational requirements. For complicated situations with larger volumes and real objects, the results would be expected to improve with an increase in the number of transducers.

In most applications only the pressure wave field is measured, which makes it interesting to start with imaging based on the scalar wave equation as formulated in Eq. (11). This equation is obtained by neglecting the presence of a velocity wave field. Consequently, the corresponding imaging algorithms are obtained by neglecting the presence and influence of the components related to the velocity wave field in Eqs. (12)–(43). During imaging, this will result in additional changes in the compressibility, in order to compensate for changes present in the density profile. Consequently, synthetic acoustic data were computed for a speed of sound profile, a cross section of which in the  $(x,y)$  plane is shown in Fig. 2(a). Note that changes in the density were neglected and compensated for by additional changes in the compressibility. A cross section of the result of the reconstruction based on the CS formulation after 512 iterations without taking the TV into account is shown in Fig. 2(b). Here, we used the expression given in Eq. (28) with  $M=1$  to obtain an estimate of the compressibility, which in combination with the known density of the background medium resulted in a speed of sound profile. Note that only three frequencies,  $n_f=3$ , equally spread over the full frequency range, were used. The error in the reconstructed speed of sound profile [see Fig. 2(c)] is small;  $|\Delta c(\mathbf{r})| \leq 0.5$  m/s, and is distributed evenly throughout the image, except for a few points at the edges of the contrasts.

In this paper, three methods were given which can be used to reconstruct speed of sound profiles from contrast sources; direct minimization via Eq. (26), and with positivity constraint via Eq. (28) for  $M=1$  and  $M=2$ . We tested the three methods on the noise-free synthetic data without taking TV into account and plotted the normalized error functionals for all three methods in Fig. 2(d). The results show that the fastest convergence is obtained with direct minimization and

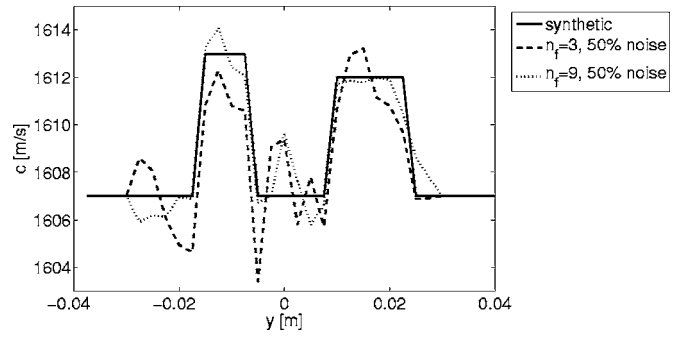


FIG. 4. A cross section of the reconstructed speed of sound profile  $c(\mathbf{r})$  along the line  $x=0$  m and  $z=0$  m. The synthetic pressure wave field and the imaging are based on changes in the compressibility only.

for  $M=1$ ; note that both lines coincide. In order to test the sensitivity of all methods to noise we added 50% complex white noise to the data, viz.,

$$\hat{p}^{\text{sct;noise}}(\mathbf{r}) = \hat{p}^{\text{sct}}(\mathbf{r}) + \nu \max(|\hat{p}^{\text{sct}}(\mathbf{r})|), \quad (44)$$

where the complex random number  $\nu$  reads  $\nu = \alpha + i\beta$ , with real numbers based on white noise in the range  $-(1/2\sqrt{2}) \leq \alpha \leq (1/2\sqrt{2})$  and  $-(1/2\sqrt{2}) \leq \beta \leq (1/2\sqrt{2})$ . Hence, the absolute value of  $\nu$  equals  $0 \leq |\nu| \leq \frac{1}{2}$ . The results for all three methods are shown in Fig. 2(e). It clearly shows that minimization with  $M=2$  has become unstable, while the remaining two methods are stable and behave comparably. Finally, we increased the number of frequencies from  $n_f=3$  to  $n_f=9$ . This stabilized the process slightly as can be observed from Fig. 2(f). The results can be explained if we replace in Eqs. (26) and (28) the reconstructed contrast source  $\hat{w}_{N;k}^p(\mathbf{r})$  with its corresponding value  $\hat{s}(\kappa^{\text{bg}} - \kappa_{N;k}^{\text{obj}}(\mathbf{r}))\hat{p}_{N;k}^{\text{tot}}(\mathbf{r})$  based on the computed compressibility and total pressure wave field. This leads to the following expressions for  $\kappa_N^{\text{obj}}(\mathbf{r})$ ; based on direct minimization:

$$\kappa_N^{\text{obj}}(\mathbf{r}) = \frac{\sum_{k,\Omega} \kappa_{N;k}^{\text{obj}}(\mathbf{r}) |\hat{s}\hat{p}_{N;k}^{\text{tot}}(\mathbf{r})|^2}{\sum_{k,\Omega} |\hat{s}\hat{p}_{N;k}^{\text{tot}}(\mathbf{r})|^2}, \quad (45)$$

based on Eq. (28) for  $M=1$

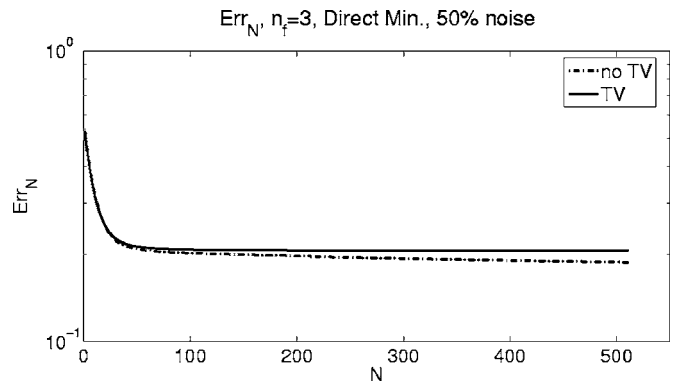


FIG. 5. The effect of total variation (TV) on the error functional  $\text{Err}_N$ .



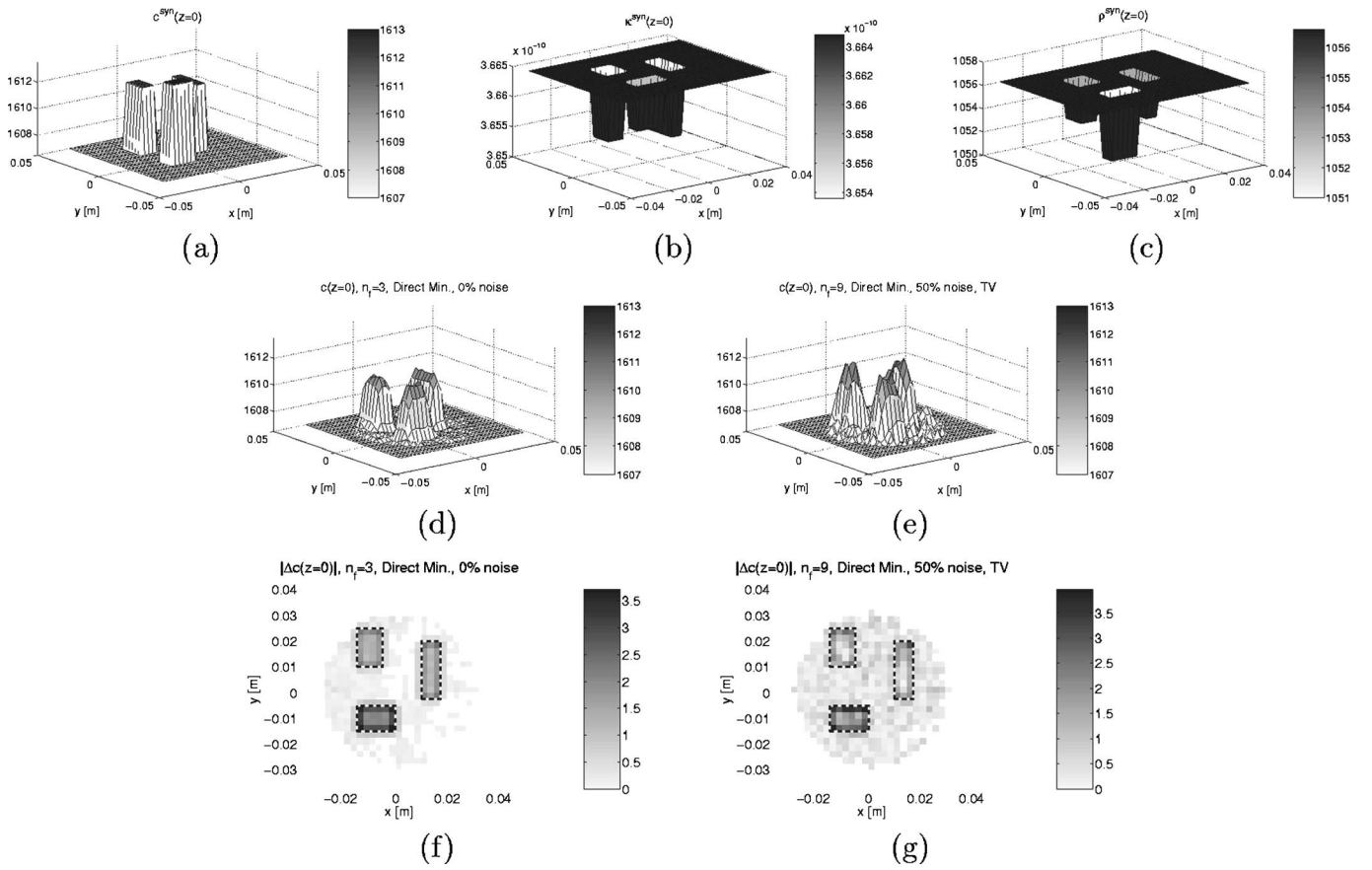


FIG. 6. Cross sections of the reconstructed speed of sound profiles  $c(\mathbf{r})$  at  $z=0$  m and the absolute errors  $|\Delta c(\mathbf{r})|$  in the reconstructions. The imaging is based on direct minimization (direct min.) using three frequencies only and direct minimization with total variation (TV) using nine frequencies when noise is present. The synthetic pressure wave field is based on changes in both compressibility and volume density of mass while the imaging is based on changes in compressibility only.

$$\kappa_N^{\text{obj}}(\mathbf{r}) = \left( \frac{\sum_{k,\Omega} [\kappa_{N;k}^{\text{obj}}(\mathbf{r})]^2 |\hat{s}_{N;k}^{\text{tot}}(\mathbf{r})|^2}{\sum_{k,\Omega} |\hat{s}_{N;k}^{\text{tot}}(\mathbf{r})|^2} \right)^{1/2}, \quad (46)$$

and based on Eq. (28) for  $M=2$

$$\kappa_N^{\text{obj}}(\mathbf{r}) = \left( \frac{\sum_{k,\Omega} [\kappa_{N;k}^{\text{obj}}(\mathbf{r})]^2}{\sum_{k,\Omega} 1} \right)^{1/2}. \quad (47)$$

Based on the large similarity between Eqs. (45) and (46), similar results are expected for these two minimization methods, while Eq. (47) is similar to taking the root-mean-square of all reconstructed values and therefore very sensitive to noise in the data.

Total variation is taken into account in order to suppress the noise present in the data. The results are shown in Fig. 3. Prior to investigating the effect of TV, we first investigated the effect of the number of frequencies used during the inversion process. For noise-free data this effect is minimal as can be observed from Figs. 3(a), 3(d), 3(g), and 3(j) and Fig. 4. However, in the presence of noise, increasing the number of frequencies results in a clear improvement in the reconstructed contrast profiles; see Figs. 3(b), 3(e), 3(h), and 3(k). Finally, TV is applied in order to regularize the problem.

This proves to be a very effective method to handle noise, as can be observed from Figs. 3(c), 3(f), 3(i), and 3(l). In addition, it is observed that the usage of TV does not always have a positive effect on the convergence speed, as can be concluded from Fig. 5. Here, a decrease in convergence speed is observed in the case data with noise is used.

In most cases, changes in speed of sound occur due to the presence of changes in both the compressibility and the density. This results in both a scattered scalar pressure and a scattered vectorial velocity wave field. Consequently, it is expected that a scalar model is not sufficient to obtain accurate speed of sound profiles. The effect of neglecting the vectorial component of the full acoustic wave equation in the reconstruction process is tested by computing synthetic data based on the same speed of sound profile as used for the previous results, but now taking changes in both compressibility and density into account; see Figs. 6(a)–6(c). Using three frequency components in the absence of noise enables the localization of all three objects, but with amplitudes which are lower than the actual synthetic values. The error in the reconstructed speed of sound profile is approximately five times bigger than the results obtained with the full scalar model. Increasing the number of frequencies corrects partly for this effect. In the case where 50% noise is present in the data and TV is applied, the error increases approximately by a factor of  $2\frac{1}{2}$  compared with the same situation where syn-

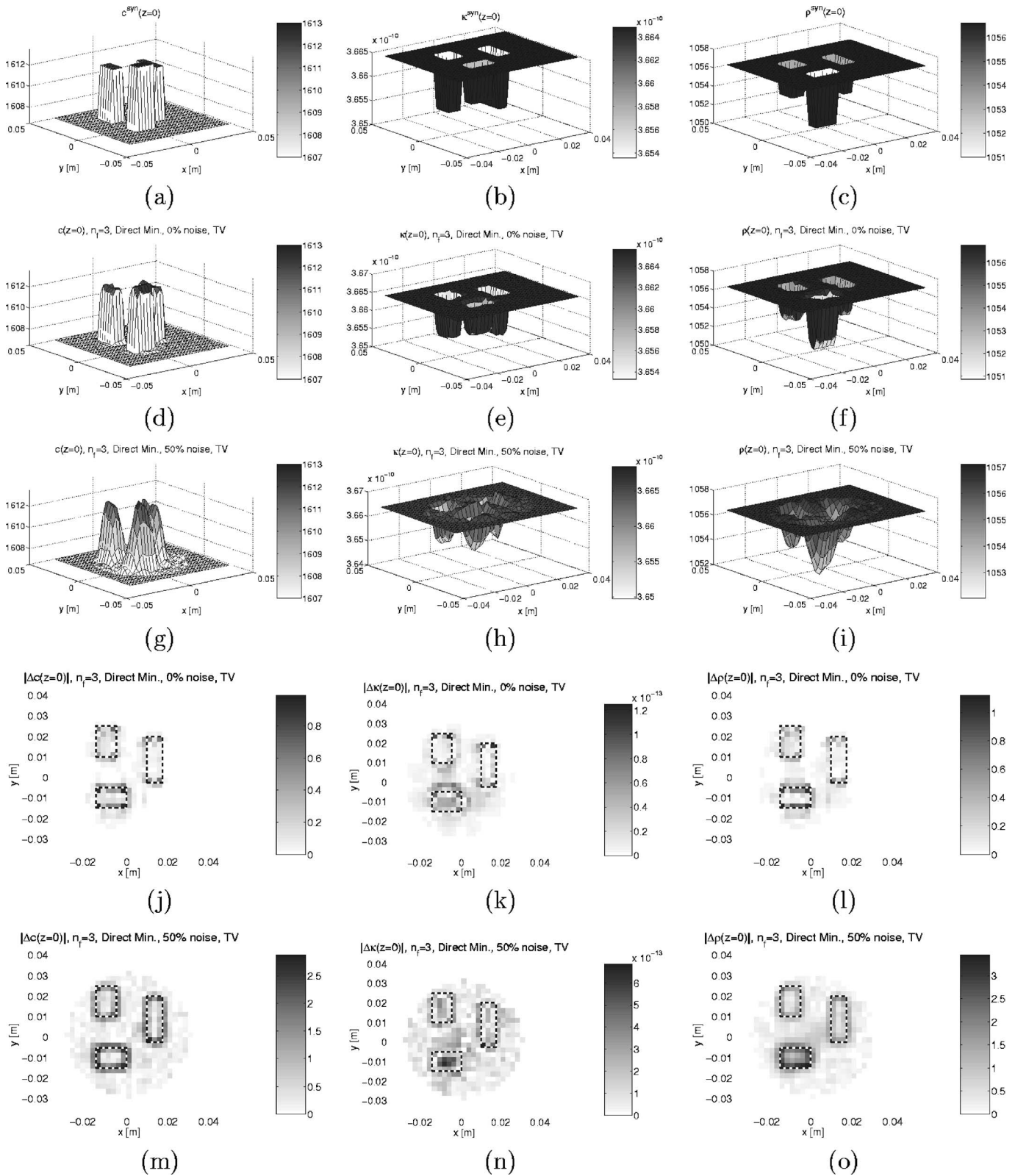


FIG. 7. Cross sections of the reconstructed speed of sound profiles  $c(\mathbf{r})$  at  $z=0$  m based on the compressibility  $\kappa(\mathbf{r})$  and density  $\rho(\mathbf{r})$  profiles, and their absolute errors. The imaging is based on direct minimization (direct min.) with total variation (TV) using three frequencies. The synthetic pressure and velocity wave field and the imaging are based on changes in both compressibility and volume density of mass.

thetic data are obtained from the scalar model. Hence, the scalar reconstruction alone is insufficient in situations where there are changes in both density and compressibility.

Finally, the full vectorial inversion scheme is tested on the same synthetic data set as discussed previously. The syn-

thetic profile was based on both changes in compressibility and density, and during the imaging both the pressure and velocity wave fields were taken into account. The results are shown in Figs. 7 and 8. In the absence of noise, a reconstructed speed of sound profile based on three frequencies is

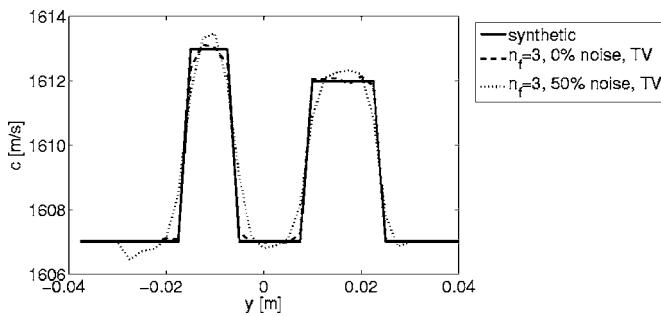


FIG. 8. A cross section of the reconstructed speed of sound profile  $c(r)$  along the line  $x=0$  m and  $z=0$  m. The synthetic pressure and velocity wave field and the imaging are based on changes in both compressibility and volume density of mass.

almost  $2\frac{1}{2}$  times as accurate as the reconstructed profile using the pressure field only; compare Fig. 6(f) with Fig. 7(j). In the presence of noise the error in the reconstruction with the full model in combination with TV based on three frequencies is still approximately  $1\frac{1}{2}$  times smaller than the error in the image based on the scalar inversion model using nine frequencies; compare Fig. 6(g) with Fig. 7(m). More importantly, the full vectorial imaging method allows the reconstruction of both density and compressibility profiles; see Figs. 7(e), 7(f), 7(h), and 7(i). Note that the obtained accuracy is excellent, even when using frequencies with corresponding wavelengths larger than the contrasts to be detected. The images could be improved further by increasing the number of nodes and frequencies, but at the expense of computational efficiency.

## V. CONCLUSION

In this paper we described a full vectorial three-dimensional inversion method based on the acoustic wave equations. The combined scalar pressure and vectorial velocity wave field description allows the reconstruction of the acoustic medium parameters compressibility and volume density of mass with a conjugate gradient contrast source (CG-CS) inversion scheme. This minimizes two error functionals in an iterative scheme. The first error functional is referred to as the data equation and relates the measured scattered acoustic wave fields to contrast sources in the volume of interest, while the second error functional is referred to as the object equation and relates the contrast sources to the contrasts and the total wave fields. The contrast profiles are obtained by applying direct minimization on the second error functional for computed total wave fields based on reconstructed contrast sources. Testing this method on synthetic measured data resulted in the reconstruction of profiles of the acoustic medium parameters compressibility and mass density in the region of interest. From these reconstructed medium parameters, speed of sound profiles are obtained in a straightforward manner. In the presence of noise, additional regularization becomes essential; it stabilizes the minimization procedure and reduces the blurring in the reconstructed contrast profiles. This regularization is obtained by taking the total variation (TV) of the reconstructed contrast profiles into account and has proven to be effective for handling data after adding 50% complex-valued white noise.

In many situations, only the pressure wave field is measured and the scalar wave equation is used as a starting point for computing speed of sound profiles. Therefore, we also developed a contrast source inversion scheme for pressure wave fields only. We tested the algorithms for two situations based on the same speed of sound profile: (i) a profile based solely on changes in the compressibility, and (ii) a profile based on changes in both the compressibility and density. In both situations the imaging method using only the pressure wave field was successful in localizing the contrasts; however, the amplitude of the reconstructed speed of sound profile in the second case, with the combined contrast, was lower than the amplitude of the synthetic profile or the reconstructed profile in the case where there was only a contrast in compressibility.

To conclude, in situations where changes in speed of sound are caused by changes in both compressibility and volume density of mass, it is still possible to obtain speed of sound profiles by using pressure wave fields only. The results improve significantly by using the full vectorial acoustic wave equation, which enables the use of both the velocity and the pressure wave field, and allows the reconstruction of both acoustic medium parameters density and compressibility. The three-dimensional CG-CS method with TV as an additional regularization tool is an effective method to obtain these results with good resolution.

## ACKNOWLEDGMENTS

This work was supported by Marie Curie Intra-European Fellowship Number MEIF-CT-2003-501333. We also gratefully acknowledge the Boole Centre for Research in Informatics, University College Cork, Ireland, for the usage of their computer facility.

- <sup>1</sup>S. J. Norton and M. Linzer, "Ultrasonic reflectivity imaging in three dimensions: Exact inverse scattering solutions for plane, cylindrical, and spherical apertures," *IEEE Trans. Biomed. Eng.* **28**(2), 202–220 (1981).
- <sup>2</sup>J. F. Greenleaf and R. C. Bahn, "Clinical imaging with transmissive ultrasonic computerized-tomography," *IEEE Trans. Biomed. Eng.* **28**(2), 177–185 (1981).
- <sup>3</sup>A. J. Devaney, "A filtered back-propagation algorithm for diffraction tomography," *Ultrason. Imaging* **4**(4), 336–350 (1982).
- <sup>4</sup>H. W. Jones, "Recent activity in ultrasonic tomography," *Ultrasonics* **31.5**, 353–360 (1993).
- <sup>5</sup>S. A. Johnson, D. A. Christensen, C. C. Johnson, J. F. Greenleaf, and B. Rajagopalan, "Noninvasive measurement of microwave or ultrasound induced hyperthermia by acoustic temperature tomography," *Proceedings 1977 IEEE Ultrasonics Symposium*, 977–982 (1977).
- <sup>6</sup>N. T. Sanghvi, F. J. Fry, R. Bihrl, R. S. Foster, M. H. Phillips, J. Syrus, A. V. Zaitsev, and C. W. Hennige, "Noninvasive surgery of prostate tissue by high-intensity focused ultrasound," *IEEE Trans. Ultrason. Ferroelectr. Freq. Control* **43**(6), 1099–1110 (1996).
- <sup>7</sup>J. E. Kennedy, G. R. ter Haar, and D. Cranston, "High intensity focused ultrasound: Surgery of the future?," *Br. J. Audiol.* **76**, 590–599 (2003).
- <sup>8</sup>G. Ter Haar, "Ultrasound focal beam surgery," *Ultrasound Med. Biol.* **21**, 1089–1100 (1995).
- <sup>9</sup>C. J. Diederich and K. Hynynen, "Ultrasound technology for hyperthermia," *Ultrasound Med. Biol.* **25**, 871–887 (1999).
- <sup>10</sup>N. R. Miller, J. C. Bamber, and G. R. ter Haar, "Imaging of temperature-induced echo strain: Preliminary *in vitro* study to assess feasibility for guiding focused ultrasound surgery," *Ultrasound Med. Biol.* **30**(3), 345–356 (2004).
- <sup>11</sup>R. Souchon, G. Bouchoux, E. Maciejko, C. Lafon, D. Cathignol, M. Bertrand, and J. Y. Chapelon, "Monitoring the formation of thermal lesions with heat-induced echo-strain imaging: A feasibility study," *Ultrasound*



- Med. Biol. **31**(2), 251–259 (2005).
- <sup>12</sup>N. R. Miller, J. C. Bamber, and P. M. Meaney, “Fundamental limitations of noninvasive temperature imaging by means of ultrasound echo strain estimation,” *Ultrasound Med. Biol.* **28**(10), 1319–1333 (2002).
- <sup>13</sup>K. A. Wear, R. F. Wagner, M. F. Insana, and T. J. Hall, “Application of autoregressive spectral analysis to cepstral estimation of mean scatterer spacing,” *IEEE Trans. Ultrason. Ferroelectr. Freq. Control* **40**(1), 50–58 (1993).
- <sup>14</sup>N. T. Sanghvi, R. S. Foster, F. J. Fry, R. Bihrl, C. Hennige, and L. V. Hennige, “Ultrasound intracavity system for imaging, therapy planning and treatment of focal disease,” *Proceedings IEEE Ultrasonics Symposium 1992*, **2**, 1249–1253 (October 1992).
- <sup>15</sup>R. Seip, P. VanBaren, and E. S. Ebbini, “Dynamic focusing in ultrasound hyperthermia treatments using implantable hydrophone arrays,” *IEEE Trans. Ultrason. Ferroelectr. Freq. Control* **41**(5), 706–713 (1994).
- <sup>16</sup>R. Seip and E. S. Ebbini, “Noninvasive estimation of tissue temperature response to heating fields using diagnostic ultrasound,” *IEEE Trans. Biomed. Eng.* **42**(8), 828–839 (1995).
- <sup>17</sup>A. N. Amini, E. S. Ebbini, and T. T. Georgiou, “Noninvasive estimation of tissue temperature via high-resolution spectral analysis techniques,” *IEEE Trans. Biomed. Eng.* **52**(2), 221–228 (2005).
- <sup>18</sup>T. D. Mast, “Empirical relationships between acoustic parameters in human soft tissues,” *ARLO* **1**(2), 37–42 (2000) and references herein.
- <sup>19</sup>J.-W. Jeong, T.-S. Kim, D. C. Shin, S. Do, M. Singh, and V. Z. Marmarelis, “Soft tissue differentiation using multiband signatures of high resolution ultrasonic transmission tomography,” *IEEE Trans. Med. Imaging* **24**(3), 399–408 (2005).
- <sup>20</sup>Y. Nawata, and K. Kaneko, “Measurement of temperature distribution in phantom body by an ultrasonic CT method,” *Proceedings of the ASME/JSME Joint Thermal Engineering Conference* **3**, 469–474 (1999).
- <sup>21</sup>D. Kourtiche, M. Nadim, G. Kontaxakis, C. Marchal, and G. Prieur, “Temperature measurements using US tomography: Theoretical aspects,” *Proceedings of the Annual International Conference of the IEEE Engineering in Medicine and Biology Society Proc. IEEE Eng. Med. Biol. Soc.* **13**(1), 325–326 (1991).
- <sup>22</sup>K. W. A. van Dongen and W. M. D. Wright, “A forward model and conjugate gradient inversion technique for low-frequency ultrasonic imaging,” *J. Acoust. Soc. Am.* **120**, 2086 (2006); **120**(4), 2086–2095 (2006).
- <sup>23</sup>A. T. de Hoop, *Handbook of Radiation and Scattering of Waves: Acoustic Waves in Fluids, Elastic Waves in Solids, Electromagnetic Waves* (Academic, London, 1995).
- <sup>24</sup>P. M. van den Berg, “Iterative schemes based on minimization of a uniform error criterion,” *PIERS 5, Application of Conjugate Gradient Method to Electromagnetics and Signal Analysis*, edited by T. K. Sarkar (Elsevier, New York, 1991), pp. 27–66.
- <sup>25</sup>R. E. Kleinman and P. M. van den Berg, “Iterative methods for solving integral equations,” *PIERS 5, Application of Conjugate Gradient Method to Electromagnetics and Signal Analysis*, edited by T. K. Sarkar (Elsevier, New York, 1991), pp. 67–102.
- <sup>26</sup>R. E. Kleinman and P. M. van den Berg, “A modified gradient method for two-dimensional problems in tomography,” *J. Comput. Appl. Math.* **42**, 17–35 (1992).
- <sup>27</sup>P. M. van den Berg and R. E. Kleinman, “A total variation enhanced modified gradient algorithm for profile reconstruction,” *Inverse Probl.* **11**, L5–L10 (1995).
- <sup>28</sup>R. Acar and C. R. Vogel, “Analysis of bounded variation penalty methods for ill-posed problems,” *Inverse Probl.* **10**, 1217–1229 (1994).
- <sup>29</sup>S. Osher and L. Rudin, “Feature-oriented image enhancement using shock filters,” *SIAM (Soc. Ind. Appl. Math.) J. Numer. Anal.* **27**, 919–940 (1990).
- <sup>30</sup>L. Rudin, S. Oshet, and C. Fatemi, “Nonlinear total variation based noise removal algorithm,” *Physica D* **60D**, 259–268 (1992).
- <sup>31</sup>T. M. Habashy, M. L. Oristaglio, and A. T. de Hoop, “Simultaneous nonlinear reconstruction of two-dimensional permittivity and conductivity,” *Radio Sci.* **29**, 1101–1118 (1994).
- <sup>32</sup>R. E. Kleinman and P. M. van den Berg, “An extended range modified gradient technique for profile inversion,” *Radio Sci.* **28**, 877–884 (1993).
- <sup>33</sup>R. E. Kleinman and P. M. van den Berg, “Two-dimensional location and shape reconstruction,” *Radio Sci.* **29**, 1157–1169 (1994).
- <sup>34</sup>P. M. van den Berg and R. E. Kleinman, “A contrast source inversion method,” *Inverse Probl.* **13**, 1607–1620 (1997).
- <sup>35</sup>P. M. van den Berg and A. Abubakar, “Inverse scattering algorithms based on contrast source integral representations,” *Inverse Probl. Eng.* **10**, 559–576 (2002).
- <sup>36</sup>P. M. van den Berg and A. Abubakar, “Contrast Source Inversion Method: State of Art,” in *PIER 34, Electromagnetic Waves*, edited by J. A. Kong (EMW, Cambridge, MA, 2001), pp. 189–218.
- <sup>37</sup>G. Pelekanos, A. Abubakar, and P. M. van den Berg, “Contrast source inversion methods in elastodynamics,” *J. Acoust. Soc. Am.* **114**(5), 2825–2834 (2003).
- <sup>38</sup>A. Abubakar, T. M. Habashy, P. M. van den Berg, and D. Gisolf, “The diagonalized contrast source approach: An inversion method beyond the Born approximation,” *Inverse Probl.* **21**(2), 685–702 (2005).
- <sup>39</sup>A. Abubakar and P. M. van den Berg, “Iterative forward and inverse algorithms based on domain integral equations for three-dimensional electric and magnetic objects,” *J. Comput. Phys.* **195**, 236–262 (2004).
- <sup>40</sup>P. M. van den Berg and A. Abubakar, “Contrast source inversion of 3D objects with electric and magnetic contrasts,” *2004 URSI/EMTS Proceedings of the International Symposium on Electromagnetic Theory*, 700–702 (2004).
- <sup>41</sup>K. W. A. van Dongen and W. M. D. Wright, “A contrast source inversion scheme for imaging acoustic contrast,” *Proceedings IEE Irish Signals and Systems Conference*, Dublin, Ireland, 1–2 September, 278–283 (2005).
- <sup>42</sup>A. J. Devaney, “Variable density acoustic tomography,” *J. Acoust. Soc. Am.* **78**(1), 120–130 (1985).
- <sup>43</sup>M. Moghaddam and W. C. Chew, “Simultaneous inversion of compressibility and density in the acoustic inverse problem,” *Inverse Probl.* **9**, 715–730 (1993).
- <sup>44</sup>S. Mensah and J. P. Lefebvre, “Enhanced compressibility tomography,” *IEEE Trans. Ultrason. Ferroelectr. Freq. Control* **44**(6), 1245–1252 (1997).
- <sup>45</sup>K. Fisher, S. Lehman, and D. Chambers, “Development of a multiview time-domain imaging algorithm with a Fermat correction,” *J. Acoust. Soc. Am.* **118**(5), 3122–3128 (2005).
- <sup>46</sup>C. Lu, W. C. Chew, and G. P. Otto, “Image reconstruction with acoustic measurement using distorted Born iterative method,” *Ultrason. Imaging* **18**, 140–156 (1996).
- <sup>47</sup>N. Bleistein and J. K. Cohen, “Nonuniqueness in the inverse source problem in acoustics and electromagnetics,” *J. Math. Phys.* **18**, 194–201 (1997).
- <sup>48</sup>J. T. Fokkema and P. M. van den Berg, *Seismic Applications of Acoustic Reciprocity* (Elsevier Science, Amsterdam, 1993).
- <sup>49</sup>P. M. van den Berg, A. Abubakar, and J. T. Fokkema, “Multiplicative regularization for contrast profile inversion,” *Radio Sci.* **38**(2), VIC 23-1-10 (2003).
- <sup>50</sup>K. W. A. van Dongen, C. Brennan, and W. M. D. Wright, “A reduced forward operator for acoustic scattering problems,” *Proceedings IEE Irish Signals and Systems Conference*, Dublin, Ireland, 1–2 September 2005, pp. 294–299 (2005).